Progress In Electromagnetics Research M, Vol. 37, 1–10, 2014

Focusing Translational Variant Bistatic Forward-Looking SAR Data Based on Two-Dimensional Non-Uniform FFT

Chan Liu[1], Shunsheng Zhang[1, *], Chunyang Dai[2], and Ji Zhou[1]

Abstract—Forward-looking imaging has extensive potential applications, such as self-navigation and self-landing. By choosing proper geometry, bistatic synthetic aperture radar (BiSAR) can break through the limitations of monostatic SAR on forward-looking imaging and provide possibility of the forward-looking imaging. In this special bistatic configuration, two problems involving large range cell migration (RCM) and large range-azimuth coupling are introduced by the forward-looking beam, which make it difficult to use traditional data focusing algorithms. To address these problems, a novel Omega-K algorithm based on two-dimensional non-uniform FFT (2-D NUFFT) for translational variant (TV) bistatic forward-looking SAR (BFSAR) imaging is proposed in this paper. In this study, we derive an accurate spectrum expression based on two-dimensional principle of stationary phase (2-D POSP). 2-D NUFFT is utilized to eliminate the range-variant term, which can make full use of the data and improve the computational efficiency as well. The experimental results, presented herein, demonstrate the effectiveness and advantages of the proposed algorithm.

1. INTRODUCTION

Synthetic aperture radar is a radar imaging technology, which is capable of producing high resolution images of an observed area under all-time and all-weather [1]. In some applications, such as military and aircraft landing systems, a forward-looking imaging radar is highly desirable. However, traditional monostatic SAR is not applicable in forward direction due to azimuth ambiguities and poor Doppler resolution. To improve the Doppler resolution and avoid azimuth ambiguities simultaneously, BiSAR in principle provides the possibility of the forward-looking image by choosing proper geometry [2–4].

In recent years, some valuable studies on BiSAR image formation have been proposed, which can be divided into two categories: time domain and frequency domain. Time-domain methods can focus bistatic SAR data well, but these methods always have huge computational costs. The processing efficiency can be highly improved in the frequency domain, where the bistatic point target reference spectrum (BPTRS) is an important basis [5–7]. However, the existence of the double square root (DSR) term in the bistatic range makes it difficult to get the exact solution for the two-dimensional (2-D) spectrum. Approximate solutions to get 2-D spectrum have been researched, such as the method of series reversion (MSR) [5], Loffeld's bistatic formula (LBF) [8, 9], extended LBF (ELBF) [6, 12], and two-dimensional principle of stationary phase (2-D POSP) [10, 11]. Among these methods, 2-D POSP can be utilized to achieve an approximate one-to-one correspondence between time and Doppler frequency, thereby formulating an accurate BPTRS.

The bistatic forward-looking SAR (BFSAR) employs the spatially separated forward-looking receiver and side-looking transmitter. Some theories for BFSAR have been developed in [13–16]. In [13], BFSAR is categorized into three types: translational invariant (TI), translational variant (TV), and stationary transmitter cases. In the TV cases, the transmitter and receiver platforms are moving along

Received 5 April 2014, Accepted 9 June 2014, Scheduled 13 June 2014

* Corresponding author: Shunsheng Zhang (zhangss.bit@gmail.com).

[1] Research Institute of Electronic Science and Technology, University of Electronic Science and Technology of China, Chengdu, Sichuan 611731, China. [2] Institute of Electronics, Chinese Academy of Sciences, Beijing 100864, China.

different trajectories with different velocities. Compared with the other two cases, TV-BFSAR is more flexible and can be used for reconnaissance, guidance and so on. However, in TV-BFSAR, the large range-azimuth coupling and large range cell migration (RCM) are the major problems. Moreover, the spatial variations of TV-BFSAR raw data have 2-D characteristics. Hence, many algorithms used in BiSAR cannot focus TV-BFSAR data well, and choosing proper imaging method is a key issue. In [10], range-Doppler algorithm (RDA) and chirp scaling algorithm (CSA) based on 2-D POSP for BiSAR is proposed. But the spatial variations of the Doppler parameters in the azimuth direction are ignored, which causes significant performance degradation of RCM correction and azimuth compression. Zhang and Li [14] introduce a novel RDA for BFSAR configuration. However, owing to the approximation of the phase history, the focusing accuracy is severely affected. Additionally, this method is only able to get narrow-swath BFSAR image. An Omega-K imaging algorithm for TI-BiSAR has been proposed in [17]. But the one-dimensional (1-D) Stolt interpolation used in [17] can only eliminate the spatial variations in the range direction. Due to the 2-D spatial variation characteristics, this algorithm is no longer applicable for TV-BFSAR imaging. Using ELBF, an Omega-K algorithm for BiSAR is presented in [12]. For the range-variant term, it adopts 2-D Stolt interpolation to correct the nonlinear dependence on the range and azimuth frequencies. 2-D Stolt interpolation transforms the non-uniform frequency domain into a regular spaced rectangle [18, 19]. For TV mode, the imaging block size becomes very small, leading low utilization of the collected data in the spatial frequency domain. Hence, this method based on Stolt interpolation is not applicable for TV-BFSAR any more.

Non-uniform FFT (NUFFT) is an accurate and efficient technique to evaluate the non-uniform discrete Fourier transform (NUDFT) [19–23]. Recently, NUFFT technique was introduced to the research field of SAR data processing [19, 21, 22]. In this paper, a novel Omega-K algorithm based on 2-D NUFFT for TV-BFSAR imaging is proposed. Based on the accurate spectrum expression derived by using 2-D POSP, 2-D NUFFT is utilized to compute the optimum reconstruction image, and comes at low computational cost scaled with complexity $O(MN\log_2 MN)$. Compared with the Omega-K method presented in [12], the proposed algorithm can make full efficient use of the collected data in the spatial frequency domain. Performance comparisons of the proposed algorithm with the algorithms in [10, 12] are conducted to demonstrate the advances of the Omega-K algorithm presented in this paper. The rest of this paper is organized as follows. The signal model of BFSAR is established in Section 2. In Section 3, the spectrum derived using 2-D POSP is rewritten and a novel Omega-K algorithm based on 2-D NUFFT is proposed. Section 4 conducts the performance comparisons of the proposed algorithm with conventional algorithms. The conclusions of the paper are drawn in Section 5.

2. SIGNAL MODEL

Figure 1 shows the imaging geometry of the bistatic forward-looking SAR, including parallel tracks and unequal velocities. The receiving antenna is forward looking, while the transmitter antenna is squint looking. The scene center is set to be the origin of coordinates and the height of the scene is assumed to be zero.

After demodulation to baseband, the received signal can be expressed by the range time τ and azimuth time η

$$s(\tau,\eta) = p\left(\tau - \frac{R(\eta)}{c}\right) \times \exp\left(-j2\pi\frac{R(\eta)}{\lambda}\right) \tag{1}$$

where c represents the speed of light and λ the carrier wavelength. $p(\cdot)$ is defined as the transmitted signal, and the instantaneous range history $R(\eta)$ is given by

$$R(\eta) = R_T(\eta) + R_R(\eta) \tag{2}$$

where

$$\begin{aligned} R_T(\eta) &= \sqrt{{R_{0T}}^2 + (\eta - \eta_{0T})^2 {v_T}^2} \\ R_R(\eta) &= \sqrt{{R_{0R}}^2 + (\eta - \eta_{0R})^2 {v_R}^2} \end{aligned} \tag{3}$$

here R_{0T} is the minimum slant range from transmitter to scene center and R_{0R} the height of receiver. η_{0T} and η_{0R} stand for initial offset time of transmitter and receiver, respectively. The moving velocities of transmitter and receiver are respectively denoted by v_T and v_R.

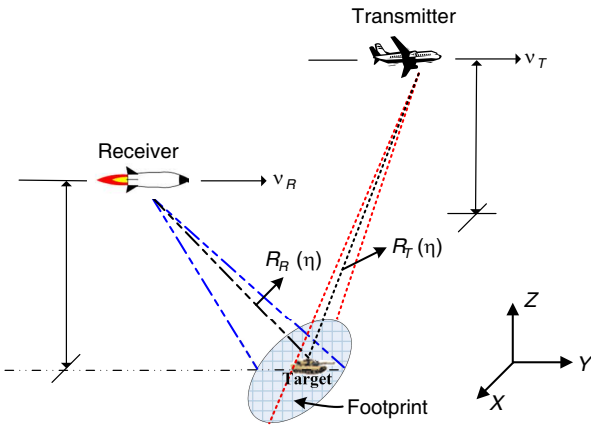

Figure 1. Imaging geometry of bistatic forward-looking SAR.

3. IMAGE FORMATION ALGORITHM

3.1. Rewriting The Signal Spectrum

2-D FFT is made toward (1) using 2-D POSP [10], then ignore the amplitude, the spectrum expression of bistatic forward-looking echo signal can be described as

$$S(f_\tau, f_\eta) = p(f_\tau) \exp[-j\varphi(f_\tau, f_\eta)] \tag{4}$$

where

$$\varphi(f_\tau, f_\eta) = 2\pi(f_{\eta T}\eta_{0T} + f_{\eta R}\eta_{0R}) + 2\pi\left[\frac{R_{0T}}{c}F_{TW} + \frac{R_{0R}}{c}F_{RW}\right] \tag{5}$$

$$\begin{aligned}
F_{TW} &= \sqrt{(f_\tau + f_0)^2 - \left(\frac{cf_{\eta T}}{v_T}\right)^2} & F_{RW} &= \sqrt{(f_\tau + f_0)^2 - \left(\frac{cf_{\eta R}}{v_R}\right)^2} \\
f_{\eta T} &= k_T(f_\eta - f_{DcR} - f_{DcT}) + f_{DcT} & f_{\eta R} &= k_R(f_\eta - f_{DcR} - f_{DcT}) + f_{DcR} \\
f_{DcT} &= \frac{v_T \sin\theta_{ST}}{c/(f_\tau + f_0)} & f_{DcR} &= \frac{v_R \sin\theta_{SR}}{c/(f_\tau + f_0)} \\
k_T &= \frac{k_{\eta T}}{k_{\eta T} + k_{\eta R}} & k_R &= \frac{k_{\eta R}}{k_{\eta T} + k_{\eta R}} \\
k_{\eta T} &= \frac{v_T^2 \cos^3\theta_{ST}}{\lambda R_{0T}} & k_{\eta R} &= \frac{v_R^2 \cos^3\theta_{SR}}{\lambda R_{0R}}
\end{aligned} \tag{6}$$

where f_τ and f_η stand for the range and azimuth frequency, respectively. f_0 is the carrier frequency of the transmitted signal. The squint angles of transmitter and receiver at the composite beam center crossing time are respectively denoted by θ_{ST} and θ_{SR}.

To facilitate the development of processing algorithms, we bilinearly express η_{0T}, R_{0T}, and R_{0R} in terms of (r, η_{0R}) [9].

$$\begin{aligned}
\eta_{0T} &= p_{10} + p_{11}r + p_{12}\eta_{0R} \\
R_{0T} &= p_{20} + p_{21}r + p_{22}\eta_{0R} \\
R_{0R} &= r + R_m
\end{aligned} \tag{7}$$

where R_m is the closest range from the scene center to the ideal trajectory of receiver and $r = R_{0R} - R_m$.

Substituting (7) into (5), the phase history can be expressed as

$$\begin{aligned}
\varphi(f_\tau, f_\eta) \approx{}& 2\pi[p_{10} + p_{11}(r + R_m)]k_T f_\eta + 2\pi(p_{12}k_T + k_R)\eta_{0R}f_\eta + \frac{2\pi}{c}(r + R_m)F_{RW} \\
&+ \frac{2\pi}{c}(p_{20} + p_{21}r + p_{22}\eta_{0R})F_{TW} + \frac{2\pi}{c}(k_T v_R \sin\theta_{SR} - k_R v_T \sin\theta_{ST})(f_\tau + f_0)[(1 - p_{12})\eta_{0R} - p_{10} - p_{11}r]
\end{aligned} \tag{8}$$

Similar to [8], (8) can be decomposed into two components: QM phase term and BD phase term.

$$\varphi\left(f_\tau, f_\eta\right) = \varphi_{QMW}\left(f_\tau, f_\eta\right) + \varphi_{BDW}\left(f_\tau, f_\eta\right) \tag{9}$$

where

$$\begin{aligned}\varphi_{QMW}\left(f_\tau, f_\eta\right) &= 2\pi p_{10} k_T f_\eta + 2\pi p_{11} r k_T f_\eta + 2\pi\left(p_{12} k_T + k_R\right)\eta_{0R} f_\eta \\ &\quad + \frac{2\pi}{c} p_{22}\eta_{0R} F_{TW} + \frac{2\pi}{c}\left(r + R_m\right) F_{RW} + \frac{2\pi}{c}\left(p_{20} + p_{21} r\right) F_{TW}\end{aligned} \tag{10}$$

$$\varphi_{BDW}\left(f_\tau, f_\eta\right) = \frac{2\pi}{c}\left(k_T v_R \sin\theta_{SR} - k_R v_T \sin\theta_{ST}\right)\left(f_\tau + f_0\right)\left(\eta_{0R} - \eta_{0T}\right) + 2\pi p_{11} R_m k_T f_\eta \tag{11}$$

From (10), it can be readily shown that $2\pi p_{22}\eta_{0R} F_{TW}/c$ contains an azimuth-dependent range cell migration (RCM) term which is introduced by the azimuth-variant baseline between transmitter and receiver. For clarity, we expand F_{TW} with respect to f_τ and f_η as

$$\frac{2\pi}{c} p_{22}\eta_{0R} F_{TW} \approx \frac{2\pi}{c} p_{22}\eta_{0R}\left[\sqrt{f_0^2 - \left(\frac{c f_{dc}}{v_T}\right)^2} + \frac{\left(\frac{c f_{dc}}{v_T}\right)^2}{\sqrt{f_0^2 - \left(\frac{c f_{dc}}{v_T}\right)^2}} + \frac{f_\tau}{\sqrt{1 - \left(\frac{\lambda f_{dc}}{v_T}\right)^2}} - \frac{\left(\frac{c}{v_T}\right)^2 f_{dc}}{\sqrt{f_0^2 - \left(\frac{c f_{dc}}{v_T}\right)^2}} f_\eta\right] \tag{12}$$

where $f_{dc} = v_R \sin\theta_{SR}/\lambda + v_T \sin\theta_{ST}/\lambda$. In (12), the first two terms denote the residual phase terms and are negligible; the third term is the azimuth-dependent RCM and the last term represents the azimuth-scaling term [9]. Therefore, (10) and (11) can be rewritten as

$$\tilde{\varphi}_{QMW}\left(f_\tau, f_\eta\right) = 2\pi p_{10} k_T f_\eta + 2\pi p_{11} r k_T f_\eta + \frac{2\pi}{c}\left(r + R_m\right) F_{RW} + \frac{2\pi}{c}\left(p_{20} + p_{21} r\right) F_{TW} + 2\pi\beta_\eta\eta_{0R} f_\eta \tag{13}$$

$$\tilde{\varphi}_{BDW}\left(f_\tau, f_\eta\right) = \varphi_{BDW}\left(f_\tau, f_\eta\right) + \frac{2\pi p_{22}\eta_{0R} f_\tau}{c\sqrt{1 - \left(\frac{\lambda f_{dc}}{v_T}\right)^2}} \tag{14}$$

where

$$\beta_\eta = p_{12} k_T + k_R - \frac{\lambda p_{22} f_{dc}}{v_T^2\sqrt{1 - \left(\frac{\lambda f_{dc}}{v_T}\right)^2}} \tag{15}$$

3.2. Omega-K Algorithm Based on 2-D NUFFT

To deal with $\tilde{\varphi}_{BDW}$, we perform a preprocessing operation in the range-azimuth subsections to remove it. The preprocessing function is given as

$$H_{pre}\left(f_\tau, f_\eta\right) = \exp\left[j\tilde{\varphi}_{BDW}\left(f_\tau, f_\eta\right)\right] \tag{16}$$

For further clarity, $\tilde{\varphi}_{QMW}$ is decomposed into a range-invariant term, range-variant term and azimuth-scaling term [12]. Hence, (13) can be expressed as

$$\tilde{\varphi}_{QMW}\left(f_\tau, f_\eta\right) = \phi_1\left(f_\tau, f_\eta\right) + \phi_2\left(f_\tau, f_\eta\right) + \phi_{AS}\left(f_\eta\right) \tag{17}$$

where

$$\phi_1\left(f_\tau, f_\eta\right) = 2\pi p_{10} k_T f_\eta + \frac{2\pi}{c} R_m F_{RW} + \frac{2\pi}{c} p_{20} F_{TW} \tag{18}$$

$$\phi_2\left(f_\tau, f_\eta\right) = 2\pi\frac{\left(1 + p_{21}\right) r}{c}\frac{\left(c p_{11} k_T f_\eta + F_{RW} + p_{21} F_{TW}\right)}{\left(1 + p_{21}\right)} \tag{19}$$

$$\phi_{AS}\left(f_\eta\right) = 2\pi\beta_\eta\eta_{0R} f_\eta \tag{20}$$

$\phi_1(f_\tau, f_\eta)$ represents the range-invariant component. It can be removed with reference function multiplication (RFM) in the 2-D frequency domain. $\phi_{AS}(f_\eta)$ is the azimuth-scaling term. In this paper, the correction factor for $\phi_{AS}(f_\eta)$ is substituted by averaged values over slant range and azimuth time. Thus, the azimuth-scaling term can also be corrected with RFM in the 2-D frequency domain. The RFM filter is obtained as following

$$H_{RFM}\left(f_\tau, f_\eta\right) = \exp\left\{j\left[\phi_1\left(f_\tau, f_\eta\right) + \phi_{AS}\left(f_\eta\right)\right]\right\} p^*\left(f_\tau\right)\exp\left(-j2\pi\frac{R_m + p_{20}}{c} f_\tau\right) \tag{21}$$

The last exponential term of (21) denotes a phase correction to establish the phase reference to the scene center.

$\phi_2(f_\tau, f_\eta)$ stands for the range-variant component, which contains the range-variant RCM, range-azimuth coupling and azimuth modulation. Obviously, it is significant to correct $\phi_2(f_\tau, f_\eta)$ in a subsequent operation to focus precisely over the whole scene. The coupling between f_τ and f_η can be removed if we rescale f_τ by the frequency mapping

$$f'_\tau = \frac{(cp_{11}k_T f_\eta + F_{RW} + p_{21}F_{TW})}{(1+p_{21})} - f_0 \tag{22}$$

After mapping operation, the data from (f_τ, f_η) space to (f'_τ, f_η) space, (19) can be converted to

$$\phi_2(f_\tau, f_\eta) = 2\pi \frac{(1+p_{21})\, r}{c}(f'_\tau + f_0) \tag{23}$$

It can be readily shown from (22) that the range-azimuth coupling can be eliminated and RCM can be sufficiently corrected. However, due to non-uniform distribution of the spatial frequencies f'_τ and f_η, the focused image cannot be obtained only by 2-D inverse FFT (IFFT). Stolt interpolation is in general utilized to solve this problem, which transforms the 2-D non-uniform frequency domain into a regular spaced rectangle. Then 2-D IFFT is employed to generate an image [17]. This method inevitably makes the supported domain small and decreases the data utilization. Using the simulation parameters defined in Section 4, the non-uniform distribution of the spatial frequencies f'_τ and f_η is showed in Fig. 2. In this kind of TV-BFSAR case, the method based on Stolt interpolation can only utilize a small part (the red rectangle in Fig. 2) in the skew 2-D support. Obviously, the data utilization is quite low, which affects the image performance severely.

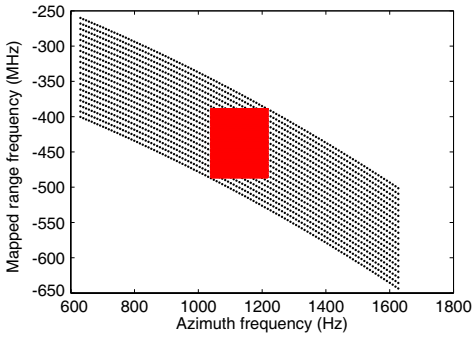

Figure 2. Frequency samples point in (f'_τ, f_η) space.

NUFFT is an accurate and efficient technique to evaluate the non-uniform discrete Fourier transform (NUDFT) [19–23]. According to [20], the reconstruction of target scattering function can be represented by

$$I_{k,l} = \sum_{m=0}^{M-1}\sum_{n=0}^{N-1}\left[S_{m,n}\exp\left(j\frac{2\pi}{M}k\tilde{\alpha}_{m,n} + j\frac{2\pi}{N}l\tilde{\beta}_{m,n}\right)\right] \quad -M/2 \le k < M/2, \quad -N/2 \le l < N/2 \tag{24}$$

where

$$S_{m,n} = S(m\Delta f_\tau, n\Delta f_\eta) \tag{25}$$

$$\tilde{\alpha}_{m,n} = \frac{M\Delta x}{2\pi}\left[\alpha(m\Delta f_\tau, n\Delta f_\eta) - \alpha_0\right] \tag{26}$$

$$\tilde{\beta}_{m,n} = \frac{N\Delta y}{2\pi}\left[\beta(m\Delta f_\tau, n\Delta f_\eta) - \beta_0\right] \tag{27}$$

where Δx, Δy, Δf_τ and Δf_η denote the sampling interval in X-axis, Y-axis, range frequency and azimuth frequency, respectively. M and N represent the number of sampling points in range frequency and azimuth frequency. After RFM, the signal in the 2-D frequency domain is denoted by S. α and β is the spatial frequencies f'_τ and f_η. (α_0, β_0) is the midpoint of the irregular spatial frequencies region.

According to [20], 2-D NUFFT can substitute for Stolt interpolation and 2-D IFFT to get the focused image, but also can effectively utilize the echo information. Additionally, the direct computing of (24), a two-dimensional discrete Fourier transform process, takes $O(M^2N^2)$ arithmetical operations, while 2-D NUFFT based on Least-Square can compute the same result in only $O(MN\log_2 MN)$ operations which is the same to the complexity for the algorithm based on 2-D POSP in [10] and the omega-k algorithm in [12]. Hence, 2-D NUFFT for BFSAR image formation is a good balance between computational load and focusing performance. The processing of the proposed algorithm consists of the following steps.

(1) Using 2-D POSP, 2-D spectrum expression is generated.
(2) Based on bilinear regression and Taylor expansion, the phase history is rewritten, and it can be expressed as QM term and BD term.
(3) Preprocessing operation to deal with the BD term.
(4) RFM to remove the range-invariant component and the azimuth-scaling term.
(5) Mapping operation to eliminate the range-azimuth coupling and correct the RCM.
(6) 2-D NUFFT operation to linearize both 2-D frequency and obtain the focused image.

4. SIMULATION RESULTS

The purpose of the simulation is to verify the effectiveness of the proposed imaging algorithm. The simulation parameters are listed in Table 1. Firstly, point scatterers simulation is conducted to validate the proposed algorithm in this paper. Then, we apply the traditional methods in [10, 12] to BFSAR configuration. Performance comparisons of the proposed algorithm with the traditional methods demonstrate that the former can focus TV-BFSAR better.

Table 1. Simulation radar parameters.

Transmitter initial location	$(-3, 0, 8)$ km	Carrier frequency	9.65 GHz
Receiver initial location	$(0, -2, 4)$ km	Range bandwidth	100 MHz
Velocity of transmitter	200 m/s	PRF	1000 Hz
Velocity of receiver	100 m/s	Pulse width	10 μs

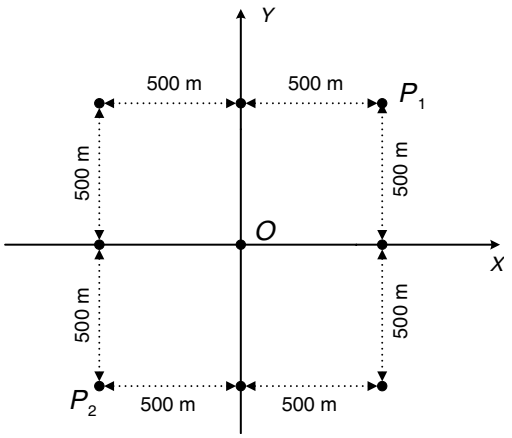

Figure 3. Location of point targets for simulation.

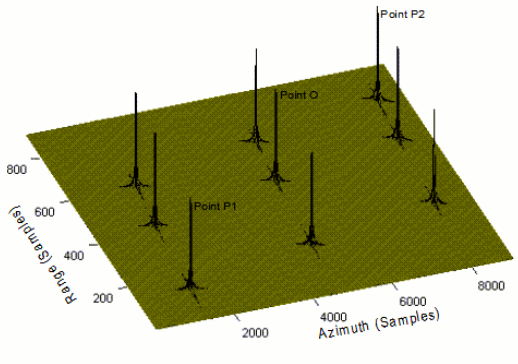

Figure 4. Two-dimensional spatial-domain result after the 2-D NUFFT operation.

4.1. Point Scatterers Simulation

The simulated scenario consists of nine point targets in the ground plane $z = 0$, which is shown in Fig. 3. The reference point O is located at the center of the scene, and the other eight points are all located in a 1100 m $\times$ 1100 m square. Among the nine point targets, P_1 is the furthest-range point target, and P_2 is the shortest-range point target. Using the parameters of Table 1, the nine point targets are reconstructed via the proposed algorithm. The result is shown in Fig. 4. Obviously, 2-D NUFFT accomplishes range-azimuth coupling correction and RCM correction.

4.2. Performance Comparisons

A smaller scenario (300 m $\times$ 300 m) is chosen to test the algorithms in order to compare the focused performance of the algorithms in more detail. In this scenario, points $A(100, 100)$, $B(0, 0)$, $C(-100, -100)$ are analyzed to quantify the imaging precision of the proposed algorithm. In order to show the details, the results are interpolated by a factor of 16. Figs. 5(a)–(c) give the contours of points A, B, and C processed by the proposed Omega-K algorithm. Comparatively, Figs. 5(d)–(f) give the contours of points A, B, and C processed by the algorithm based on ELBF in [12], and Figs. 5(g)–(i) give those contours processed by the RD algorithm based on 2-D POSP in [10]. In Fig. 5, the horizontal axis and the vertical axis are range samples and azimuth samples, respectively. By the simulation

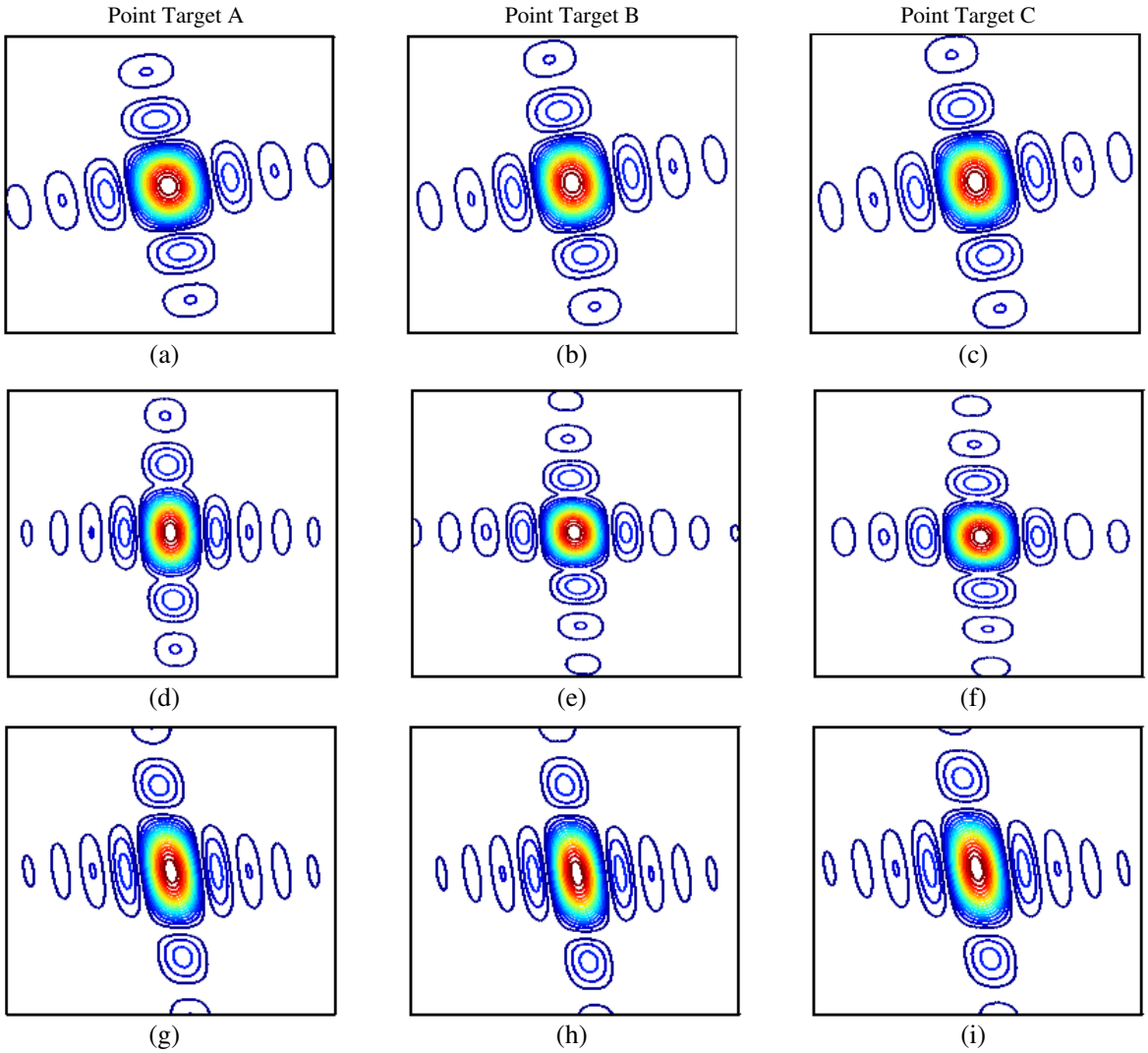

Figure 5. Contours of points A, B, and C in the 300 m $\times$ 300 m square. (a)–(c) Processed by the proposed method. (d)–(f) Processed by the method in [12]. (g)–(i) Processed by the method in [10].

results, it is clear that the proposed algorithm and the RD algorithm based on 2-D POSP in [10] can fully focus all the targets at the same time, whereas simulation results of the method in [12] is not so well.

On the other hand, points P_1, O, and P_2 in the 1100 m × 1100 m square are also analyzed in detail. Similarly, Fig. 6 respectively give the contours of points P_1, O, and P_2 processed by the proposed Omega-K algorithm, and the methods in [10, 12]. In Fig. 6, the horizontal axis and the vertical axis are range samples and azimuth samples, respectively. The simulation results show that the algorithm proposed in this paper can fully focus all the targets at the same time. By contrast, the methods in [10, 12] can focus the target at the reference position well, whereas targets at the corners of scenario are only partially focused.

In order to evaluate the reconstructed point target at the corner of scenario, the Peak Side-Lobe Ratio (PSLR) and the Integrated Side-Lobe Ratio (ISLR) are utilized as measurement of performance, and the evaluation results of target P_1 are tabulated in Table 2. In addition, the azimuth profiles with respect to target P_1 are shown in Fig. 7, where the red solid line, green solid line, and blue dotted line represent the results using the proposed method in this paper and the methods in the literatures, respectively [10, 12]. It can be seen that the proposed algorithm in this paper has good focusing performance, whereas the focusing performance of the imaging algorithm in [12] and the method in [10]

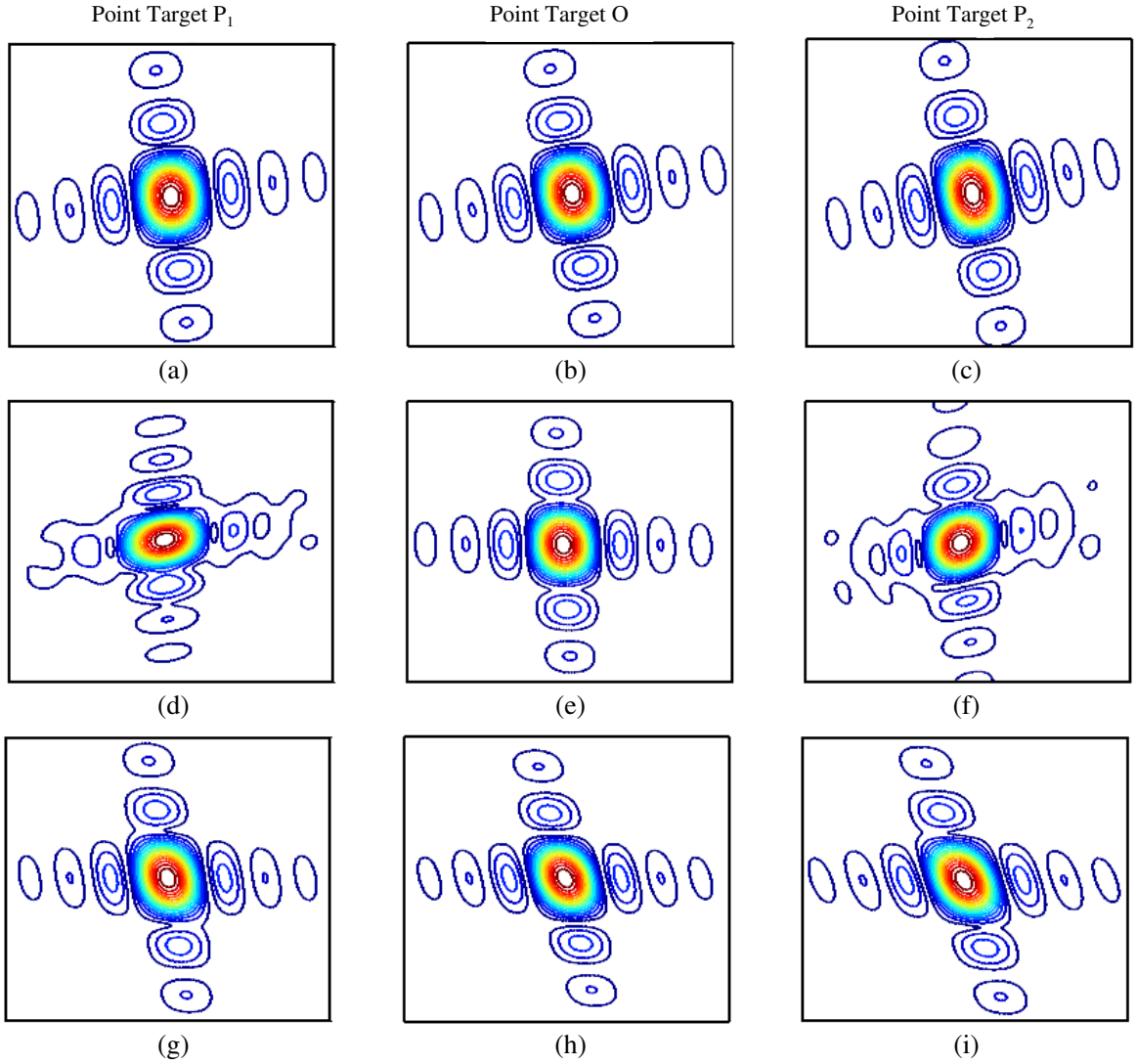

Figure 6. Contours of points P_1, O, and P_2 in the 1100 m × 1100 m square. (a)–(c) Processed by the proposed method. (d)–(f) Processed by the method in [12]. (g)–(i) Processed by the method in [10].

Table 2. Imaging performance of P_1.

	Range		Azimuth	
	PSLR (dB)	ISLR (dB)	PSLR (dB)	ISLR (dB)
The proposed method	−13.26	−10.69	−13.13	−11.00
The method in [12]	−14.05	−13.67	−13.82	−10.90
The method in [10]	−13.31	−9.67	−12.93	−10.61

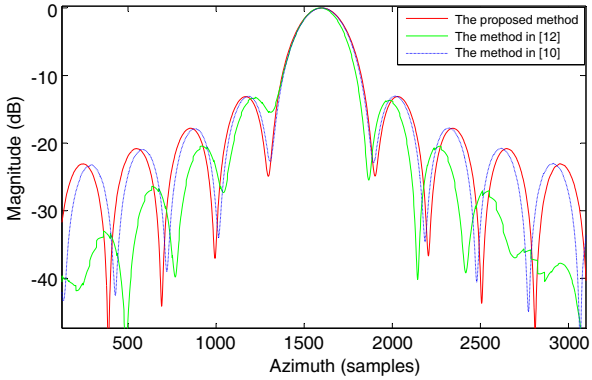

Figure 7. Azimuth profiles of targets P_1.

is not so well.

The simulation results for different scenarios indicate that the proposed algorithm in this paper has nearly ideal focusing performance, even in a large scenario. However, the imaging algorithm of Wang [12] has bad imaging results mainly because the approximate spectrum based on ELBF and the utilization of Stolt interpolation make the algorithm unsuitable for TV-BFSAR. Due to ignoring the spatial variations of the Doppler parameters in the azimuth direction, the RD algorithm based on 2-D POSP in [10] can focused well in a small scene, whereas it can only partially focus targets at the corners of a large scenario. Thus, if the method in [10] is applied to BFSAR configuration, it is limited to small scenarios.

5. CONCLUSIONS

This paper presents a novel Omega-K imaging algorithm for translational variant bistatic forward-looking SAR imaging. The core of the Omega-K algorithm is to obtain the precise spectrum based on 2-D POSP, and eliminate the range-azimuth coupling and correct the RCM using 2-D NUFFT. NUFFT calculates complex kernels based on the given sampling pattern to minimize the interpolation error, and scales with complexity $O(MN\log_2 MN)$. The simulation results validate that the proposed algorithm has the ability to focus TV-BFSAR data within a 1100 m × 1100 m region. Moreover, performance comparisons prove that the imaging results of 2-D NUFFT processing have nearly ideal focusing performance with low computational cost.

REFERENCES

1. Chan, Y. K. and V. C. Koo, "An introduction to synthetic aperture radar (SAR)," *Progress In Electromagnetics Research B*, Vol. 2, 27–60, 2008.
2. Balke, J., "Field test of bistatic forward-looking synthetic aperture radar," *Proc. Record of the IEEE 2005 Int. Radar Conf.*, 424–429, 2005.
3. Walterscheid, I., T. Espeter, J. Klare, and A. Brenner, "Bistatic spaceborne-airborne forward-looking SAR," *Proc. of EUSAR*, 986–989, 2010.

4. Espeter, T., I. Walterscheid, J. Klare, A. R. Brenner, and J. H. G. Ender, "Bistatic forward-looking SAR: Results of a spaceborne-airborne experiment," *IEEE Geoscience and Remote Sensing Letters*, Vol. 8, No. 4, 765–768, 2011.
5. Neo, Y. L., F. Wong, and I. G. Cumming, "A two-dimensional spectrum for bistatic SAR processing using series reversion," *IEEE Geoscience and Remote Sensing Letters*, Vol. 4, No. 1, 93–96, 2007.
6. Wang, R., O. Loffeld, Q. Ul-Ann, et al., "A bistatic point target reference spectrum for general bistatic SAR processing," *IEEE Geoscience and Remote Sensing Letters*, Vol. 5, No. 3, 517–521, 2008.
7. Wu, J. J., J. Y. Yang, Y. L. Huang, Z. Liu, and H. G. Yang, "A new look at the point target reference spectrum for bistatic SAR," *Progress In Electromagnetics Research*, Vol. 119, 363–379, 2011.
8. Loffeld, O., H Nies, V. Peters, and S. Knedlik, "Models and useful relations for bistatic SAR processing," *IEEE Transactions on Geoscience and Remote Sensing*, Vol. 42, No. 10, 2031–2038, 2004.
9. Natroshvili, K., O. Loffeld, H. Nies, A. Medrano-Ortiz, and S. Knedlik, "Focusing of general bistatic SAR configuration data with 2-D inverse scaled FFT," *IEEE Transactions on Geoscience and Remote Sensing*, Vol. 44, No. 10, 2718–2727, 2006.
10. Wang, R., Y. K. Deng, O. Loffeld, et al., "Processing the azimuth-variant bistatic SAR data by using monostatic imaging algorithms based on two-dimensional principle of stationary phase," *IEEE Transactions on Geoscience and Remote Sensing*, Vol. 49, No. 10, 3504–3520, 2011.
11. Li, J., S. S. Zhang, and J. F. Chang, "Bistatic forward-looking SAR imaging based on two-dimensional principle of stationary phase," *Proc. of MMWCST*, 107–110, 2012.
12. Wang, R., O. Loffeld, H. Nies, and J. H. G. Ender, "Focusing spaceborne/airborne hybrid bistatic SAR data using wavenumber-domain algorithm," *IEEE Transactions on Geoscience and Remote Sensing*, Vol. 47, No. 7, 2275–2283, 2009.
13. Wu, J. J., J. Y. Yang, Y. L. Huang, H. G. Yang, and H. C. Wang, "Bistatic forward-looking SAR: Theory and challenges," *Proc. Record of the IEEE 2009 Int. Radar Conf.*, 1–4, 2009.
14. Zhang, S. S. and J. Li, "Forward-looking bistatic SAR imaging based on high order range equation and high order phase compensation," *Journal of Electromagnetic Waves and Applications*, Vol. 26, Nos. 17–18, 2304–2314, 2012.
15. Qiu, X. L., D. H. Hu, and C. B. Ding, "Some reflections on bistatic SAR of forward-looking configuration," *IEEE Geoscience and Remote Sensing Letters*, Vol. 5, No. 4, 735–739, 2008.
16. Wu, J. J., Z. Y. Li, Y. L. Huang, J. Y. Yang, H. G. Yang, and Q. H. Liu, "Focusing bistatic forward-looking SAR with stationary transmitter based on Keystone transform and nonlinear chirp scaling," *IEEE Geoscience and Remote Sensing Letters*, Vol. 11, No. 1, 148–152, 2014.
17. Liu, B., T. Wang, Q. Wu, and Z. Bao, "Bistatic SAR data focusing using an omega-k algorithm based on method of series reversion," *IEEE Transactions on Geoscience and Remote Sensing*, Vol. 47, No. 8, 2899–2912, 2009.
18. Xiong, T., M. D. Xing, X. G. Xia, and Z. Bao, "New applications of Omaga-K algorithm for SAR data processing using effective wavelength at high squint," *IEEE Transactions on Geoscience and Remote Sensing*, Vol. 51, No. 5, 3156–3169, 2013.
19. Han, K., C. C. Chen, D. D. Shen, F. Pan, et al., "An accurate 2-D nonuniform fast Fourier transform method applied to high resolution SAR image reconstruction," *Proc. of Metamaterials*, 1–4, 2012.
20. Dai, C. Y. and X. L. Zhang, "Bistatic polar format algorithm based on NUFFT method," *Journal of Electromagnetic Waves and Applications*, Vol. 25, Nos. 17–18, 2328–2340, 2011.
21. Andersson, F., R. Moses, and F. Natterer, "Fast Fourier methods for synthetic aperture radar imaging," *IEEE Transactions on Aerospace and Electronic Systems*, Vol. 48, No. 1, 215–229, 2012.
22. Liu, Z., J. Y. Yang, X. L. Zhang, H. Huang, and W. C. Li, "Imaging algorithm based on least-square NUFFT method for spaceborne/airborne squint mode bistatic SAR," *Proc. of IGARSS*, 396–399, 2012.
23. Liu, Q. H. and N. Nguyen, "An accurate algorithm for nonuniform fast Fourier transforms (NUFFT's)," *IEEE Microwave and Guided Wave Letters*, Vol. 8, No. 1, 18–20, 1998.